# Strain-induced high Chern number topological insulator state in Fe- or V-decorated MoS$_2$ monolayers

Siyavash Moradi [*] and Ali Sadeghi [†]

*Department of Physics, Shahid Beheshti University, Tehran 1983969411, Iran*

The electronic structure and topological state of an MoS$_2$ monolayer decorated by iron or vanadium adatoms is investigated by first-principles calculations. It is shown that several Chern insulator phases occur in these samples in the presence of external strain or electric field. In particular, Chern number $\mathcal{C} = 2$ is achieved by applying 6% biaxial tensile strain on the V-decorated MoS$_2$ monolayer or 10% on the Fe-decorated one. On the other hand, the intrinsic $\mathcal{C} = 1$ phase of the iron system is switched to the normal insulator phase under an electric field of 0.8 V/Å, while the vanadium system with intrinsic $\mathcal{C} = -1$ state adopts a $\mathcal{C} = 1$ state if the electric field reaches 0.7 V/Å. The induced band inversion may coincide with an abrupt increase of magnetization and a simultaneous change in the adatom adsorption height, or a magnetization decrement without displacement of the adatom. Our findings suggest that applying an in-plane biaxial tensile strain is a promising direction to search high Chern number states.

## I. INTRODUCTION

In the presence of a strong external magnetic field, the Hall conductance of a two-dimensional (2D) electron system would take on an integer [1] or a fractional [2] multiple of conductance quantum $e^2/h$, where $e$ and $h$ denote the elementary charge and Planck constant, respectively. On the other hand, the quantum anomalous Hall (QAH) effect originates from the intrinsic magnetization of the sample [3] with no need of external strong magnetic fields. The QAH effect was realized first in magnetically doped thin film topological insulators [4] but then also in three-dimensional samples [5]. The QAH phase exhibits the essential physics of the quantum Hall effect including robust dissipationless quantized conducting edge states. This phase is identified by a nonzero Chern number $\mathcal{C}$ due to the broken time reversal symmetry in the occupied bands [6,7]. QAH is known also as the *Chern insulator* state in comparison to the normal insulator ($\mathcal{C} = 0$) phase. A nonzero quantum Hall conductivity $\sigma_{xy} = \mathcal{C}(e^2/h)$, namely the existence of the edge states, leads to interesting electronic and magnetoelectric effects and applications [8].

Early experiments on, e.g., a thin slab of $(\text{Bi}, \text{Sb})_2\text{Te}_3$ doped with Cr atoms [4] were restricted to the $\mathcal{C} = \pm 1$ phase. From a practical point of view, however, a *high* Chern number phase enjoys a greater number of dissipationless chiral edge modes to carry low-noise current at the system boundary and finds application in, e.g., multichannel quantum computing [9]. Moreover, the normal electric resistance when connecting the device to the ordinary metal electrodes can be reduced by increasing the number of edge modes, i.e., $\mathcal{C}$ [10]. Therefore, searching for simples routes to achieve high-$\mathcal{C}$ QAH phases, as exemplified in the following, is of great interest. In the Haldane model for a 2D system [11], introducing electron hopping beyond the next-nearest neighbors increases the number of Dirac points and thus $\mathcal{C}$ [12–16]. Simulations with electric circuits promise the possibility of achieving arbitrarily large Chern number by including more long-range couplings [17]. The observation of a $\mathcal{C} = 2$ quantum Hall effect without Landau levels and $\mathcal{C} = 1$ Chern insulator state with nearly quantized Hall resistance plateau above the Néel temperature in MnBi$_2$Te$_4$ devices provided a new perspective on topological matter and opened up new avenues for the exploration of exotic topological quantum states and topological phase transitions at higher temperatures [18]. A QAH state with $\mathcal{C} = \pm 2$ was predicted for CrO$_2$/TiO$_2$ [19] and VO$_2$/TiO$_2$ [20] heterostructures. Multilayer structures consisting of alternating magnetically doped and undoped topological insulator layers [21,22] or normal insulator layers [23] are also shown to lead to high-$\mathcal{C}$ phases. Tight-binding modeling predicts a *tunable-$\mathcal{C}$* QAH effect by doping a topological insulator film with magnetic elements [24] where dopant concentration and film thickness serve as tuning parameters [25]. *Ab initio* calculations followed by experimental realization of an intrinsic antiferromagnetic topological insulator make a high-temperature QAH effect accessible [26]. Intercalating hBN sheets between the van der Waals layers of magnetic MnBi$_2$Te$_4$ is shown to lead to a high-$\mathcal{C}$ QAH state where $\mathcal{C}$ equals the number of the stacked magnetic layers [10]. Finally, the Chern number can be *tuned* via the arrangement of the layers in the twisted double bilayer graphene system so that $\mathcal{C} = 4$ and 2 can be generated in the AB-AB and AB-BA stacking, respectively, if the valley splitting is significant and large enough to open a gap at half filling of the first conduction band [27].

---

[*]Present address: Technical University of Munich, TUM School of Natural Sciences, Department of Chemistry, Lichtenbergstraße 4, D-85748 Garching, Germany.

[†]ali_sadeghi@sbu.ac.ir

On the other hand, scalar relativistic effects and lattice distortion have been shown to play a central role in band inversion, suggesting that searching for topological insulators could be focused also on these two mechanisms besides the band splitting due to the spin-orbit coupling (SOC) [28]. For example, *ab initio* calculations with considering SOC and Hubbard interactions predict a Chern insulator phase without band inversion for the $MoS_2$ monolayers on which V or Fe adatoms are adsorbed [29]. We take these two test cases to explore nontrivial topological properties when the layer is exposed to an external electric field or strain. A normal-to-plane electric field is shown to lead to band inversion while the Chern number remains 1 or becomes zero. We further show that a biaxial tensile strain results in a $\mathcal{C} = 2$ phase due to band inversion in the two model systems. Applying an in-plane strain is a common practical method to induce band inversion in 2D systems [28,30].

The rest of this paper is structured as follows. We first introduce the model system and the computational techniques. The results are then presented in Sec. III and discussed in Sec. IV, followed by drawing our conclusions in Sec. V.

## II. COMPUTATIONAL MODEL AND METHODS

Electronic structure calculations are performed within the framework of the density functional theory (DFT) [31,32]. Core electrons are treated with the projector augmented wave (PAW) [33] method while valance and semicore electrons ($4p^6$ $4d^5$ $5s^1$ for Mo, $2s^2$ $4p^4$ for S, $3p^6$ $3d^4$ $4s^1$ for V, and $3d^7$ $4s^1$ for Fe) are considered explicitly when expanding the wave function in terms of a basis set of plane waves up to an energy cutoff of 400 eV. The exchange-correlation functional within the Perdew-Burke-Ernzerhof (PBE) [34] form of the generalized gradient approximation (GGA) is used. The on-site Coulomb correction [35,36] is considered with Hubbard and exchange parameters $U = 3.0$ eV and $J = 0.9$ eV adapted from a previous study on the same systems [29]. The partial density of states (PDOS) is determined from collinear calculations where the magnetization is limited to up- and down-spin states. All other calculations are noncollinear in which SOC is taken into account for the Fe and V atoms.

As depicted in Fig. 1, a $3 \times 3$ supercell with the experimental lattice constant 3.16 Å [37] is employed to model the adsorption of transition metal (TM) atoms on the $MoS_2$ monolayer. We assume that the interaction between the adatom and its periodic images is negligible due to the large distance between two TM adatoms in adjacent supercells ($\sim 10$ Å) and the height of the interlayer vacuum region (18 Å). Momentum space is sampled on an $8 \times 8 \times 1$ mesh using the Monkhorst-Pack method. A biaxial tensile strain is applied as a homogeneous in-plane expansion of the layer. When an external electric field is applied normal to the layer plane, a compensating dipole sheet is included according to the so-called dipole correction method [38]. Structural relaxation is iterated until the force on every atom becomes smaller than 0.01 eV/Å. The total energy convergence criterion is set to $10^{-5}$ eV.

We characterize the topological properties of the 2D samples by the gauge-invariant Berry curvature in the momentum space, $\Omega^z(\mathbf{k})$. To this aim, we employ the VASPBERRY code
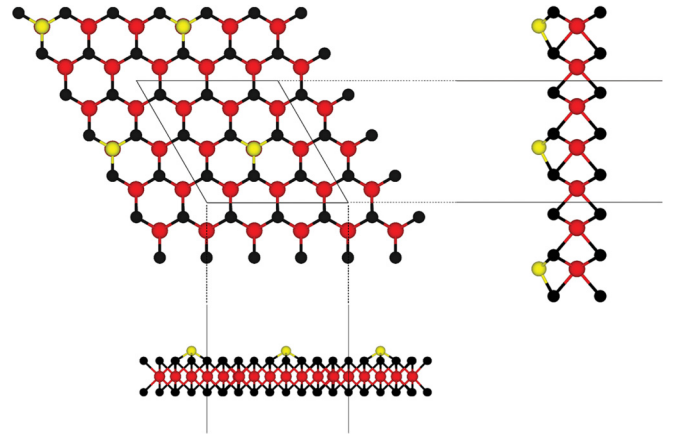


FIG. 1. Top and side views of Fe or V adatoms (yellow spheres) in their energetically most favorable adsorption configuration on the $MoS_2$ monolayer. The S and Mo atoms are represented by black and red spheres, respectively. The $3 \times 3$ supercell used in our calculations is indicated by dashed lines.

[39,40] which implements the Fukui method [41] to treat the Kubo formalism [42] for a discretized 2D system. The DFT computation output, including the self-consistent Bloch eigenfunctions $\psi_{n\mathbf{k}}$ on the discretized Brillouin zone (BZ) and the corresponding occupancies $f_{n\mathbf{k}}$ and eigenenergies $\varepsilon_{n\mathbf{k}}$, is used in this postprocessing step. The Berry curvature of band $n$ is expressed in terms of off-diagonal elements of the velocity matrix in the basis of the Bloch eigenfunctions,

$$\Omega_n^z(\mathbf{k}) = -2\mathrm{Im} \sum_{m \neq n} \frac{\langle \psi_{n\mathbf{k}} | v_x | \psi_{m\mathbf{k}} \rangle \langle \psi_{m\mathbf{k}} | v_y | \psi_{n\mathbf{k}} \rangle}{(\varepsilon_{m\mathbf{k}} - \varepsilon_{n\mathbf{k}})^2}. \quad (1)$$

The sum runs over all (occupied and unoccupied) states $m$ but is practically dominated by a few states with energies close to $\varepsilon_{n\mathbf{k}}$. Therefore, high peaks of Berry curvature are expected to appear over the $k_x$-$k_y$ space at the same points where small gaps are opened by, e.g., SOC. Finally, integrating the band Berry curvatures over the 2D BZ and summing over all the bands up to some given band energy $E$, one calculates the Chern number as

$$\mathcal{C}(E) = \frac{1}{2\pi} \sum_{\substack{n \\ (\varepsilon_{n\mathbf{k}} \leqslant E)}} \int_{\mathrm{BZ}} f_{n\mathbf{k}} \Omega_n^z(\mathbf{k}) \, d^2k. \quad (2)$$

## III. RESULTS

To find the adsorption site of the adatoms on the $MoS_2$ monolayer, we relaxed the complex structure starting from several initial-guess positions close to the four symmetric configurations where the TM atom sits on top of the Mo or S atom or on the middle of the Mo-S bridge, or the center of the hexagonal hollow. The Mo-top site (see Fig. 1) turned out to be the energetically most favorable configuration of both iron and vanadium-decorated layers, in agreement with previous reports [29,43]. A systematic investigation of stability of these structures requires molecular dynamics simulations at finite temperature or analyzing phonon dispersion. Here we only look at the adsorption energy,

$E_{ads} = E_{MoS_2} + E_{TM} - E_{TM/MoS_2}$, which shows how favorable the adsorption is. Note that if $E_{ads} > 0$ then dissociation of the adsorbed adatom from the layer *costs* some energy $E_{ads}$, indicating a favorable conformation. In the absence of external electric field or strain, the adsorption energy of Fe and V atoms on the Mo site turns out to be 1.03 and 1.14 eV, respectively, based on our DFT calculations. Without Hubbard correction included, however, larger adsorption energies were reported (2.30–2.43 eV and 2.46–2.60 eV for the Fe and V system, respectively) [29,43]. It is evident that on-site Coulomb repulsion reduces the binding tendency, although adsorption of the TM atoms on the MoS$_2$ layer is still favorable. Furthermore, the TM-decorated monolayers are both (i) magnetic with a dipole moment of 2 $\mu_B$ per Fe atom and 5 $\mu_B$ per V atom, and (ii) Chern insulators with $\mathcal{C} = 1$ and $-1$, respectively. Compared to the magnetic dipole moment of an isolated vanadium atom, i.e., 3 $\mu_B$, the predicted 5 $\mu_B$ per vanadium atom in a $3 \times 3$ supercell is surprisingly large. The same value is reported for the V-decorated MoS$_2$ $4 \times 4$ supercell [29] or MoSe$_2$ $4 \times 4$ supercell [44]. The observed coverage independence of the magnetic dipole moment implies that the magnetization is *localized* around the vanadium atom. To verify this, one may estimate atomic magnetic dipole moments by, e.g., calculating the integral of spin density within atomic basins such as spheres centered at the atomic positions. Liu *et al.* [44] reported 3.33 $\mu_B$ as an estimation of the dipole moment of a vanadium atom when adsorbed on the MoSe$_2$ monolayer. They attributed this small difference from the dipole moment of an isolated vanadium atom (3 $\mu_B$) to the interorbital charge transfer within the vanadium atom. Moreover, they showed that the adsorption of the V atom on the MoSe$_2$ monolayer also induces magnetizations to the layer: 0.38 $\mu_B$ on the closest Mo atom and 0.11 $\mu_B$ on each of the six next closest Mo atoms. This suggests that the layer atoms (rather than the adsorbed V atom) are responsible for the large induced magnetization after vanadium adsorption.

Next, we turn to the effect of an external electric field or strain. The adsorption energy, as well as some relevant interatomic distances, magnetic dipole moments, and Chern numbers of nontrivial gaps of the Fe- and V-decorated monolayers in response to an external normal-to-plane electric field are presented in Table I. First of all, note that the stronger the electric field (within the examined range up to 1 V/Å), the larger $E_{ads}$ and thus the stronger the binding of the TM atom to the layer. Interestingly, no appreciable change is observed in the Fe-decorated MoS$_2$ monolayer for fields weaker than 0.8 V/Å. At this field strength, however, the iron adatom is lifted by half an angstrom away from the Mo atom underneath while the iron-sulfur distance also increases slightly. Simultaneously, the magnetic dipole moment jumps from 2 to 3.6 $\mu_B$. This abrupt change in geometry and magnetism coincides with a topological transition to normal insulator. Only at 1 V/Å the system finds again a nontrivial gap with $\mathcal{C} = +1$. On the other hand, the distance of the vanadium atom to the Mo atom underneath gradually increases also by 0.6 Å as the electric field increases to 1 V/Å. Similarly to the Fe-decorated system, the magnetic and topological properties of the V-decorated layer show a sudden change: once the field strength reaches 0.7 eV/Å, the initial large magnetic dipole moment (5 $\mu_B$) decreases by 0.3 $\mu_B$ and, simultaneously, the

TABLE I. Adsorption energy, distance between the TM adatom and the Mo and S atoms of the underlying layer, magnetic dipole moment, and Chern numbers of nontrivial gaps for the Fe- and V-decorated model systems depicted in Fig. 1 subject to a range of electric fields.

| Adatom | Field (V/Å) | $E_{ads}$ (eV) | $d_{Mo}$ (Å) | $d_S$ (Å) | $\mu/\mu_B$ | $\mathcal{C}$ |
|---|---|---|---|---|---|---|
| iron | 0 | 1.03 | 2.55 | 2.15 | 2.0 | +1 |
| | 0.5 | 1.19 | 2.55 | 2.15 | 2.0 | +1 |
| | 0.6 | 1.10 | 2.56 | 2.16 | 2.0 | +1 |
| | 0.7 | 1.47 | 2.56 | 2.16 | 2.0 | +1 |
| | 0.8 | 1.80 | 3.02 | 2.32 | 3.6 | 0 |
| | 0.9 | 2.16 | 3.01 | 2.32 | 3.5 | 0 |
| | 1.0 | 2.57 | 3.01 | 2.32 | 3.4 | +1 |
| vanadium | 0 | 1.14 | 2.90 | 2.32 | 5.0 | −1 |
| | 0.5 | 1.21 | 2.92 | 2.32 | 5.0 | −1 |
| | 0.6 | 1.30 | 2.93 | 2.33 | 5.0 | −1 |
| | 0.7 | 1.52 | 2.93 | 2.33 | 4.7 | −1, −1 |
| | 0.8 | 1.80 | 2.94 | 2.33 | 4.6 | −1 |
| | 0.9 | 2.16 | 2.95 | 2.33 | 4.5 | −1, +1 |
| | 1.0 | 2.56 | 2.96 | 2.35 | 4.4 | +1 |

V-decorated layer gains a second nontrivial energy gap with $\mathcal{C} = -1$. The magnetic moment keeps decreasing slowly by enhancing the field whereas only one of the two $\mathcal{C} = -1$ gaps survives under 0.8 eV/Å, and a new $\mathcal{C} = +1$ gap is induced under 0.9 eV/Å. The latter nontrivial state is preserved under a 1 eV/Å field but the $\mathcal{C} = -1$ state is no longer present.

A biaxial tensile lattice strain also induces considerable geometric, magnetic, and topological changes in both samples, as reported in Table II. The Fe-S and Fe-Mo bond lengths and the magnetic dipole moment of the Fe system undergo sharp increments (by 0.3 Å, 0.1 Å, and 1 $\mu_B$, respectively) already under 6% strain. Then, the Fe position and magnetization remain almost unchanged by increasing the strain until a 10% strain changes the topological phase and induces a high Chern number $\mathcal{C} = 2$. On the other hand, the vanadium atom is displaced slightly and the nontrivial gap with $\mathcal{C} = -1$ is preserved when the strain on the MoS$_2$ layer increases gradually to 10%. The magnetic moment, however, starts rapidly

TABLE II. Same as Table I but when biaxial tensile strain is applied at zero electric field.

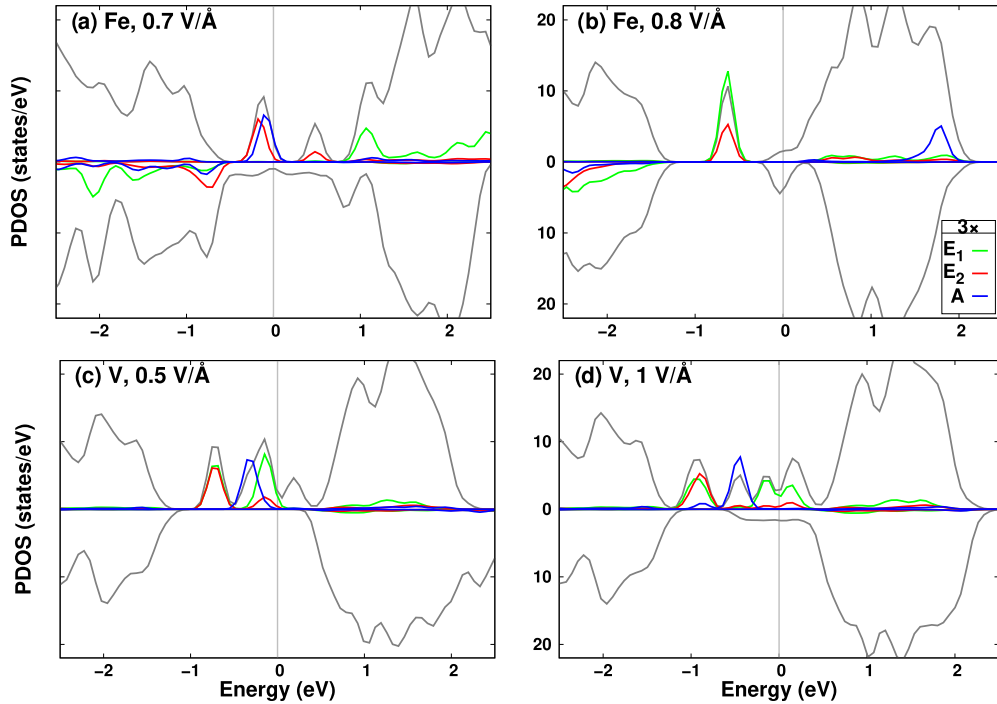| Adatom | Strain | $E_{ads}$ (eV) | $d_{Mo}$ (Å) | $d_S$ (Å) | $\mu/\mu_B$ | $\mathcal{C}$ |
|---|---|---|---|---|---|---|
| iron | 0 | 1.03 | 2.55 | 2.15 | 2.0 | +1 |
| | 0.02 | 1.04 | 2.54 | 2.17 | 2.0 | +1 |
| | 0.04 | 0.52 | 2.52 | 2.19 | 2.0 | +1 |
| | 0.06 | −0.47 | 2.82 | 2.31 | 3.0 | +1 |
| | 0.08 | −1.87 | 2.80 | 2.31 | 2.9 | +1 |
| | 0.1 | −3.72 | 2.78 | 2.32 | 2.9 | +2 |
| vanadium | 0 | 1.14 | 2.90 | 2.32 | 5.0 | −1 |
| | 0.02 | 1.20 | 2.86 | 2.33 | 5.0 | −1 |
| | 0.04 | 0.68 | 2.83 | 2.35 | 5.0 | −1 |
| | 0.06 | −0.32 | 2.85 | 2.38 | 4.6 | −1, +2 |
| | 0.08 | −1.71 | 2.86 | 2.45 | 3.9 | −1 |
| | 0.1 | −3.04 | 2.80 | 2.45 | 3.7 | −1 |

FIG. 2. Projected density of states (PDOS) from spin-polarized (no SOC) GGA+$U$ calculations for Fe (top) and V-decorated $MoS_2$ monolayer (bottom) subject to normal-to-plane electric field. Total DOS is shown by the light gray curves. For clarity, the contribution of the TM $3d$ orbitals is magnified by a factor of 3 and shown in color. The TM $d_{xz}$ and $d_{yz}$ states are labeled as $E_1$, the $d_{xy}$ and $d_{x^2-y^2}$ states by $E_2$, and the singlet state $d_{z^2}$ by $A$. Fermi energy $E_f$ is set to zero and indicated by the vertical gray line.

decreasing as the strain reaches 6%. A new $\mathcal{C} = 2$ gap appears at this strain. Note that, in contrast to electric field, tensile strain greater than 2% leads to less favorable configurations; in particular under 6% or higher strain, adsorption becomes unfavorable ($E_{ads} < 0$) and the adatom is likely disordered. It should also be noted that without SOC, the strained systems usually become metallic. Because of the essential role of SOC in this case, the gap is sometimes called a SOC gap. Finally, we do not observe a topological state change by applying *uniaxial* tensile strains up to 15%.

## IV. DISCUSSION

The results reported in Tables I and II indicate a correlated behavior of geometry, magnetization, and topological state in response to external electric field or strain. To explore the abrupt change in magnetization by electric field, we show in Fig. 2 the density of states projected on the $3d$ orbitals of the TM adatom for the relevant electric field strengths, namely 0.7 and 0.8 V/Å for the Fe-decorated monolayer (top) and 0.5 and 1 V/Å for the V system (bottom). Note that because SOC requires noncollinear magnetic calculations, we do not consider SOC in this set of calculations to determine the spin-up and spin-down contributions. Upon adsorption into the Mo-top site of the $MoS_2$ monolayer, the TM atomic orbitals adopt the $C_{3v}$ symmetry of the crystal field at the Mo-top site. Therefore, the original fivefold degenerate $3d$ orbitals of an isolated Fe or V atom are now organized as three groups. The first group is the $d_{z^2}$ state denoted by $A$, the second contains the two states $d_{xz}$ and $d_{yz}$ denoted by $E_1$, and the two states $d_{xy}$ and $d_{x^2-y^2}$ are grouped together as $E_2$. Density of states near the Fermi

level, located within the $MoS_2$ band gap, is mainly attributed to these $d$ states of the TM adatom as seen in Fig. 2 with a $3\times$ magnification for clarity. As the field strength increases from 0.7 to 0.8 V/Å, the majority spin channel of state $E_1$ of the Fe atom gains an occupied high peak while an occupied peak in the same spin channel of state $A$ disappears. Overall, the occupation of the majority spin channel of the Fe system increases with respect to the minority spin channel and the $E_1$ state of the Fe adatom is responsible for the enhanced magnetic moment from 2 to 3.6 $\mu_B$, as reported in Table I. In the case of the V-decorated monolayer, shown in Figs. 2(c) and 2(d), the strong electric field slightly suppresses the occupation peaks of $E_1$ and $E_2$ majority spin channels close to the Fermi energy while the $MoS_2$ layer states drain electrons in the opposite spin channel. The resulting 0.6 $\mu_B$ reduction of the magnetization of the V-decorated $MoS_2$ in Table I is attributed to demagnetization of both V adatom and the layer Mo atoms.

Similarly, tensile strain leads to rather significant magnetic effects. As seen in Fig. 3(a) for the Fe-decorated system in the absence of strain, the total DOS shows an occupation peak close to the Fermi energy only in the majority spin channel. This peak is entirely originated from the Fe atom $A$ and $E_2$ states and responsible for the magnetic moment of 2 $\mu_B$ according to the noncollinear calculations; see Table II. In the Fe system strained by 6%, as seen in Fig. 3(b), the iron atom $E_1$ state also contributes appreciably to the mentioned spin-up peak and induces a jump in the magnetic moment from $\mu = 2$ to 3 $\mu_B$. On the other hand, in the absence of strain the V-decorated system is highly magnetized. As seen in Fig. 3(c), all three $3d$ states of the vanadium atom contribute to the spin-up peaks close to the Fermi energy. It is
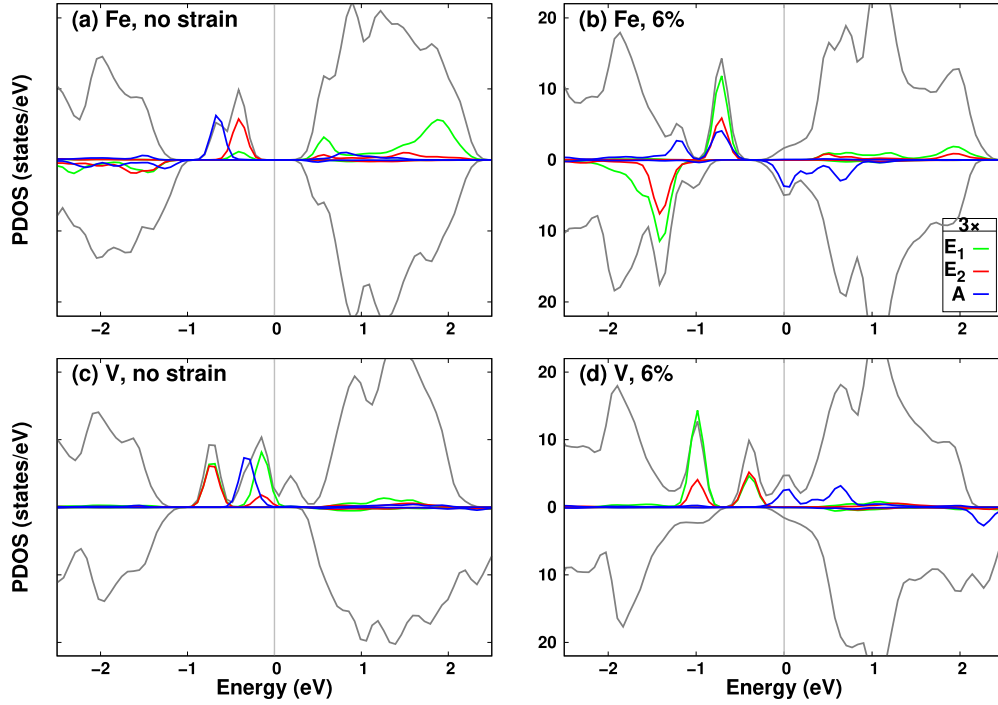
FIG. 3. Same as Fig. 2 but the samples are subject to biaxial tensile strain.

clear that the total DOS (gray curve, not magnified $3\times$) is larger than the sum of the PDOS of these three states. As mentioned earlier, the layer Mo atoms also contribute significantly in the magnetization of the V system. Figure 3(d) shows that the contribution of the vanadium $A$ state is suppressed under 6% strain while the layer is also demagnetized, in agreement with the reduction of the magnetic moment by 0.4 $\mu_B$ according to noncollinear calculations reported in Table II.

We now investigate the electronic band structure of the two model systems subject to electric field, as presented in Fig. 4. Note that the contribution of the TM $3d$ orbital is illustrated by the color bar on the right: a band that is dominantly originated

from the TM $3d$ orbital is identified by a red color while a dark blue band is assigned to the $MoS_2$ orbitals without hybridization to the TM $3d$ orbitals. If SOC is not taken into account, the two $E_1$ states are degenerate at the $\Gamma$ point although the degeneracy is lifted at any other $k$ point; the same holds true for the $E_2$ states. By considering the SOC for the Fe and V atoms, the so-called SOC gaps appear at the $\Gamma$ point, as seen in the zoom-in windows in Fig. 4, first column. The zoomed view indicates a gap (36 meV) at the $\Gamma$ point on the $E_2$ bands of the Fe-decorated monolayer although the $E_2$ bands now approach each other (down to 10 meV) along the $\Gamma$-$K$ path. Similarly, the zoomed view on the lower panel shows that the vanadium SOC also opens a tiny gap (5 meV) on the $E_1$ band
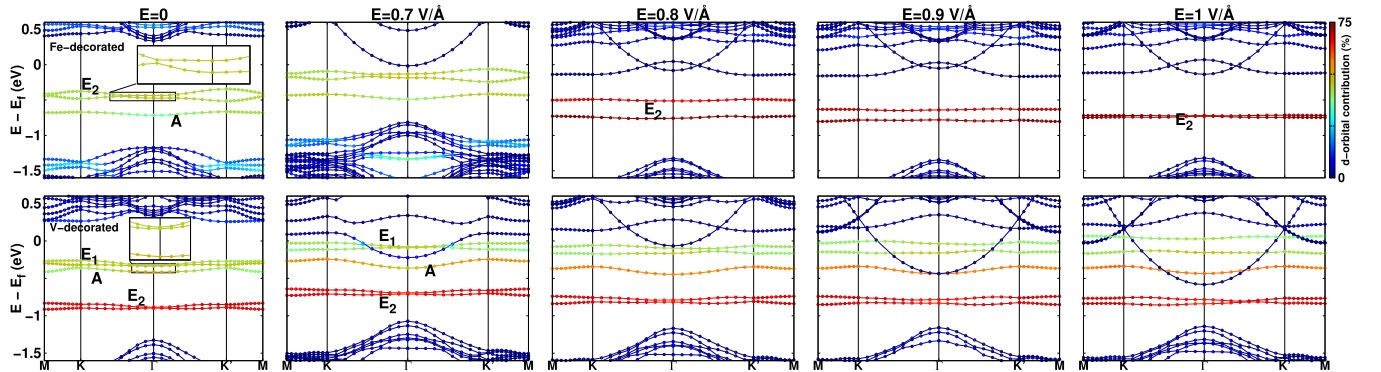
FIG. 4. Electronic energy band structure of the $MoS_2$ monolayer decorated by Fe (top) or V adatoms (bottom) adsorbed on the Mo-top site (see Fig. 1), in the absence of an external electric field (first column) or subject to normal electric field of strength 0.7 to 1 eV/Å (columns two to five, respectively). The color bar indicates the relative contribution of the $d$ orbital of the *TM adatom* labeled as $E_1$, $E_2$, and $A$ (see the text or the caption of Fig. 2). The dots represent the really calculated data while the continuous lines that connect the dots are meant to help the eye to follow the bands. Zoomed-in views of windows of height 0.1 eV are also shown in the first columns to better identify the tiny gaps. SOC is taken into account for the Fe and V atoms.
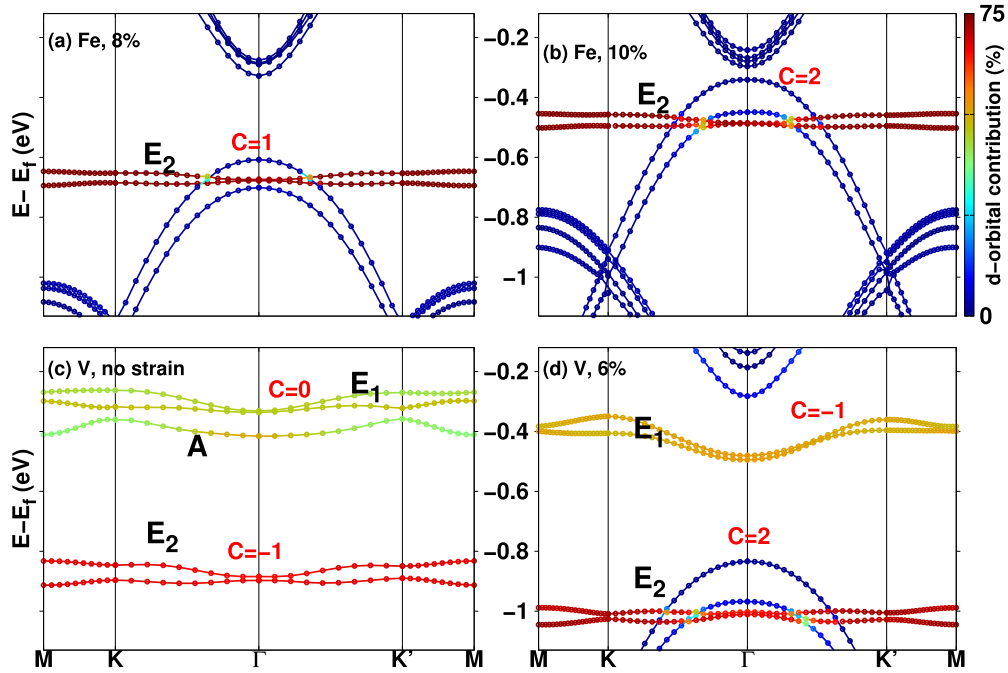
FIG. 5. Same as Fig. 4 but for applying an external in-plain tensile strain on the Fe- (top) or V-decorated MoS$_2$ monolayer (bottom). The energy axis is enlarged so that the inversion of the TM $E_2$ and Mo $d_{z^2}$ bands at the $\Gamma$ point become better visible.

at the $\Gamma$ point. The V $E_2$ band is also split (12 meV) at the $\Gamma$ point with the vanadium SOC, as clearly seen in Fig. 5(c).

So far, we have shown that the band gap opening in the $E_2$ state, originated from the iron and vanadium adatom SOC, leads to Chern insulator states with $\mathcal{C} = 1$ or $-1$, respectively. In the following we investigate how the change of the topological properties of the two samples subject to the electric field or strain, as reported in Tables I and II, can be explained in terms of band inversion. Figure 4 demonstrates the evolution of the band structures of the Fe- and V-decorated samples as a function of the field strength. The Fe system undergoes band inversion and becomes a normal insulator under a field strength of 0.8 V/Å. This transition to the trivial $\mathcal{C} = 0$ phase coincides with a considerable elongation of the Fe-Mo bond by ~0.5 Å; see Table I. Accordingly, the iron $E_2$ bands become reddish brown in the band structure diagram, meaning that this orbital is no longer hybridized with the layer atomic orbitals. Moreover, the iron $E_2$ bands become almost $k$-independent.

Despite these implying a chemical decoupling between the Fe atom and the layer, 1 V/Å induces a $\mathcal{C} = 1$ topological insulator phase. In contrast to the iron system, on the other hand, all the $3d$ states of the V adatom ($E_1$, $E_2$, and $A$) lie within the MoS$_2$ layer gap as seen in the bottom row of Fig. 4 (also clearly seen in Fig. 2 without SOC). The SOC-induced nontrivial gap between the vanadium $E_2$ bands remains open and the corresponding $\mathcal{C} = -1$ topological state is preserved unless the field is as strong as 1 V/Å. As reported in Table I, another nontrivial gap with $\mathcal{C} = -1$ is induced at field strength 0.7 V/Å, which can be attributed to the band inversion observed on the $E_1$ bands. A similar effect but with $\mathcal{C} = +1$ is present under 0.9 V/Å. The opposite signs of the two possible Chern numbers at this field strength guarantee that the direction of dissipationless edge currents is selectable

by tuning the Fermi energy to the corresponding nontrivial gap. Finally, at 1.0 V/Å, a nontrivial $\mathcal{C} = +1$ state is obtained where the vanadium $A$ band involves band inversion.

The effect of tensile strain on the topological state is also interesting because it leads to Chern numbers larger than 1. As shown in Figs. 5(a) and 5(b) for the Fe-decorated system, the minimum gap between the $E_2$ states comes back to the $\Gamma$ point in the presence of 8%–10% biaxial strain. Nevertheless, regardless of the Fe-SOC gap opening, the band inversion between the iron $E_2$ states and one or two of the MoS$_2$ states leads to $\mathcal{C} = 1$ at 8% or $\mathcal{C} = 2$ at 10% strain, respectively. In fact, the availability of two nearly degenerate $d_{z^2}$ states from the substrate molybdenum atoms has made it possible to gain a band-inversion-induced high-$\mathcal{C}$ phase. Very similar band inversion is observed for the V-decorated layer under 6% biaxial tensile strain. As shown in Fig. 5(d), a high Chern number $\mathcal{C} = 2$ state is achieved if the Fermi energy lies below the $E_1$ band. The gap above he $E_1$ band is also nontrivial and leads to a nonzero Chern number with an opposite sign, $\mathcal{C} = -1$. The same Chern number is predicted for the unstrained vanadium system for the gap between the $E_2$ and $A$ states, as seen in Fig. 5(c).

For two representative nontrivial cases, the unstrained Fe-decorated layer with $\mathcal{C} = 1$ and V-decorated layer strained by 6% with $\mathcal{C} = 2$, the distribution of the Berry curvature within the Brillouin zone (BZ)

$$\Omega_E^z(\mathbf{k}) = \sum_{\substack{n \\ (\varepsilon_{n\mathbf{k}} \leqslant E)}} f_{n\mathbf{k}} \Omega_n^z(\mathbf{k}) \qquad (3)$$

is plotted in Fig. 6. The BZ corresponds to the $3 \times 3$ supercell shown in Fig. 1 so that, apart from some asymmetry induced by the numerical noise, the Berry curvature shows the same $C_{3v}$ symmetry as the atomic structure. More
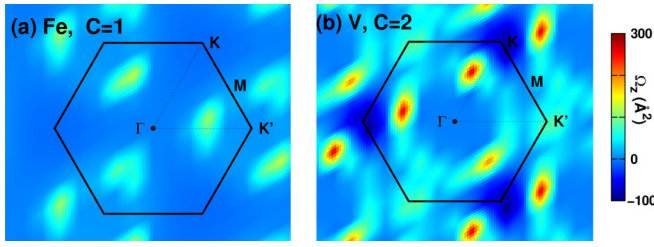
FIG. 6. Distribution of the Berry curvature $\Omega^z$ in the momentum space for the $MoS_2$ monolayer: (a) strained by 8% and decorated by iron or (b) strained by 6% and decorated by vanadium, corresponding to Figs. 5(a) and 5(d) with $\mathcal{C} = 1$ and 2, respectively. The indicated Brillouin zone corresponds to the $3 \times 3$ supercell shown in Fig. 1.

importantly, large positive peaks are established in both cases. The peaks are responsible for the nonvanishing Chern numbers $\mathcal{C}(E) = (1/2\pi) \int_{\mathrm{BZ}} \Omega_E^z(\mathbf{k}) \, d^2k$.

Note that the sum in Eq. (3) is truncated once $\varepsilon_{n\mathbf{k}} > E$. An *integer* Chern number is obtained when $E$ is set to within an energy band gap. In fact, the truncation is determined by the Fermi energy $E_f$ because the occupancies $f_{n\mathbf{k}}$ vanish for $\varepsilon_{n\mathbf{k}} > E_f$. In other words, since the sum in Eq. (3) practically runs over the *occupied* bands only, one can tune the Chern number of a material to some desired integer value by positioning the Fermi energy inside an appropriate energy gap. In particular, the realization of the high-$\mathcal{C}$ states reported in this study requires a downward shift of the Fermi energy by $\sim$0.3–0.5 eV. Such an amount of Fermi energy shift is experimentally accessible by means of, e.g., hole doping [45,46]. Based on DFT calculations, for example, a homogeneous hole doping of concentration $\sim$3.6 $\times$ 10$^{13}$ $e$/cm$^2$ decreases the Fermi energy level of the pristine $MoTe_2$ monolayer by 0.2 eV [47]. The $E_f$ of a $MoS_2$ monolayer is pushed down by 0.45 eV if an underneath graphene substrate adsorbs oxygen adatoms [48].

In the past, a number of different approaches have successfully led to generating high-$\mathcal{C}$ states. For example, in the presence of a biaxial strain and SOC, the intrinsic half-Chern insulator $Ni_2I_2$ becomes a half semiconductor, or a combined state of a half metal and a high Chern insulator is gained [49]. Achieving a $\mathcal{C} = 2$ Chern insulator state in $NiRuCl_6$ by applying a compressive biaxial strain has also been observed [50]. The on-site Coulomb repulsion $U$ or in-plane strain have been shown to change the direction of the dissipationless edge current in $LaPdO_3$ and $LaPtO_3$ bilayers [51]. Note also that high Chern numbers and Mott insulating phases have been

predicted for $BaFe_2(PO_4)_2$ by tuning the SOC and Coulomb repulsion strength [52]. We focused in this work on electric field and strain as externally driven parameters and showed, e.g., that electric field can switch the Chern number sign and strain may induce high Chern number states.

## V. CONCLUSIONS

To conclude, two Chern insulators without band inversion, Fe- and V-decorated $MoS_2$ monolayers, are exposed to in-plane strain or normal-to-plane electric field. We investigated their electronic and topological properties in terms of possible band inversions close to the Fermi energy level. The induced geometric deformations are shown to lead to band inversion. Band inversions lead to a trivial insulator phase of the Fe-decorated $MoS_2$ monolayer when the applied electric field is strong enough to change considerably the iron adatom position with respect to the neighboring Mo and S atoms. Simultaneously, the $3d$ orbital occupancy and thus the atomic magnetization change. In contrast, strong fields produce new Chern numbers in the V-decorated $MoS_2$ monolayer without inducing geometric changes but only reducing its magnetization. We identified also band inversions resulting in a high Chern number $\mathcal{C} = 2$ if 6% or 10% biaxial tensile strain is applied to the vanadium- or iron-decorated layers, respectively. The geometry and magnetization change in almost the same way as by an electric field, but the band inversion is somewhat different, and is attributed to the inversion between the molybdenum $d_{z^2}$ state and the originally degenerate vanadium $d_{xy}$ and $d_{x^2-y^2}$ states. Note that the Hall conductivity of the $\mathcal{C} = 2$ quantum anomalous Hall phase is twice that of a $\mathcal{C} = 1$ one. It is worth noting that although the structures are stable under electric fields up to 1 eV/Å according to our DFT calculations, experimentally realization of such large electric fields is not straightforward. We did not observe high-$\mathcal{C}$ states even under such strong fields. The topological character of the two Chern insulators is not affected also by uniaxial tensile tension. Overall, applying an in-plane biaxial tensile strain is suggested as a promising route of search for designing high Chern number insulators.

[1] K. v. Klitzing, G. Dorda, and M. Pepper, New method for high-accuracy determination of the fine-structure constant based on quantized Hall resistance, Phys. Rev. Lett. **45**, 494 (1980).

[2] D. C. Tsui, H. L. Stormer, and A. C. Gossard, Two-dimensional magnetotransport in the extreme quantum limit, Phys. Rev. Lett. **48**, 1559 (1982).

[3] J. Wang, B. Lian, and S.-C. Zhang, Quantum anomalous Hall effect in magnetic topological insulators, Phys. Scr. **T164**, 014003 (2015).

[4] C.-Z. Chang, J. Zhang, X. Feng, J. Shen, Z. Zhang, M. Guo, K. Li, Y. Ou, P. Wei, L.-L. Wang *et al.*, Experimental observation of the quantum anomalous Hall effect in a magnetic topological insulator, Science **340**, 167 (2013).

[5] S. Grauer, K. M. Fijalkowski, S. Schreyeck, M. Winnerlein, K. Brunner, R. Thomale, C. Gould, and L. W. Molenkamp, Scaling of the quantum anomalous Hall effect as an indicator of axion electrodynamics, Phys. Rev. Lett. **118**, 246801 (2017).

[6] D. J. Thouless, M. Kohmoto, M. P. Nightingale, and M. den Nijs, Quantized Hall conductance in a two-dimensional periodic potential, Phys. Rev. Lett. **49**, 405 (1982).

[7] A. Anirban, 15 years of topological insulators, Nat. Rev. Phys. **5**, 267 (2023).

[8] D. Zhang, M. Shi, T. Zhu, D. Xing, H. Zhang, and J. Wang, Topological axion states in the magnetic insulator $MnBi_2Te_4$ with the quantized magnetoelectric effect, Phys. Rev. Lett. **122**, 206401 (2019).

[9] X. Zhang and S.-C. Zhang, Chiral interconnects based on topological insulators, Proc. SPIE **8373**, 837309 (2012).

[10] M. Bosnar, A. Y. Vyazovskaya, E. K. Petrov, E. V. Chulkov, and M. M. Otrokov, High Chern number van der Waals magnetic topological multilayers $MnBi_2Te_4$/hBN, npj 2D Mater. Appl. **7**, 33 (2023).

[11] F. D. M. Haldane, Model for a quantum Hall effect without Landau levels: Condensed-matter realization of the parity anomaly, Phys. Rev. Lett. **61**, 2015 (1988).

[12] S. Yang, Z.-C. Gu, K. Sun, and S. Das Sarma, Topological flat band models with arbitrary Chern numbers, Phys. Rev. B **86**, 241112(R) (2012).

[13] D. Sticlet, F. Piéchon, J.-N. Fuchs, P. Kalugin, and P. Simon, Geometrical engineering of a two-band Chern insulator in two dimensions with arbitrary topological index, Phys. Rev. B **85**, 165456 (2012).

[14] D. Sticlet and F. Piéchon, Distant-neighbor hopping in graphene and Haldane models, Phys. Rev. B **87**, 115402 (2013).

[15] Y.-X. Wang, F.-X. Li, and J. Cao, The valley-degeneracy-breaking induced arbitrary-Chern number insulator on square lattice and the quantum Hall effect, J. Phys. Soc. Jpn. **84**, 024604 (2015).

[16] Y.-X. Wang, J. Cao, and Y.-M. Wu, Distant-neighbor hopping induced the Dirac points and the high Chern number topological phase on $\pi$-flux square lattice, Phys. Lett. A **379**, 2783 (2015).

[17] Z. Wang, Y. Biao, X.-T. Zeng, X. Chen, X.-L. Sheng, S. A. Yang, and R. Yu, Realization in circuits of a Chern state with an arbitrary Chern number, Phys. Rev. B **107**, L201101 (2023).

[18] J. Ge, Y. Liu, J. Li, H. Li, T. Luo, Y. Wu, Y. Xu, and J. Wang, High-Chern-number and high-temperature quantum Hall effect without Landau levels, Nat. Sci. Rev. **7**, 1280 (2020).

[19] T. Cai, X. Li, F. Wang, S. Ju, J. Feng, and C.-D. Gong, Single-spin Dirac fermion and Chern insulator based on simple oxides, Nano Lett. **15**, 6434 (2015).

[20] H. Huang, Z. Liu, H. Zhang, W. Duan, and D. Vanderbilt, Emergence of a Chern-insulating state from a semi-Dirac dispersion, Phys. Rev. B **92**, 161115(R) (2015).

[21] Y.-F. Zhao, R. Zhang, R. Mei, L.-J. Zhou, H. Yi, Y.-Q. Zhang, J. Yu, R. Xiao, K. Wang, N. Samarth *et al.*, Tuning the Chern number in quantum anomalous Hall insulators, Nature (London) **588**, 419 (2020).

[22] Y.-X. Wang and F. Li, High Chern number phase in topological insulator multilayer structures, Phys. Rev. B **104**, 035202 (2021).

[23] G. Jiang, Y. Feng, W. Wu, S. Li, Y. Bai, Y. Li, Q. Zhang, L. Gu, X. Feng, D. Zhang, and C. Song, Quantum anomalous Hall multilayers grown by molecular beam epitaxy, Chin. Phys. Lett. **35**, 076802 (2018).

[24] H. Jiang, Z. Qiao, H. Liu, and Q. Niu, Quantum anomalous Hall effect with tunable Chern number in magnetic topological insulator film, Phys. Rev. B **85**, 045445 (2012).

[25] J. Wang, B. Lian, H. Zhang, Y. Xu, and S.-C. Zhang, Quantum anomalous Hall effect with higher plateaus, Phys. Rev. Lett. **111**, 136801 (2013).

[26] M. M. Otrokov, I. I. Klimovskikh, H. Bentmann, D. Estyunin, A. Zeugner, Z. S. Aliev, S. Gaß, A. U. B. Wolter, A. V. Koroleva, A. M. Shikin *et al.*, Prediction and observation of an antiferromagnetic topological insulator, Nature (London) **576**, 416 (2019).

[27] Y.-X. Wang, F. Li, and Z.-Y. Zhang, Phase diagram and orbital Chern insulator in twisted double bilayer graphene, Phys. Rev. B **103**, 115201 (2021).

[28] Z. Zhu, Y. Cheng, and U. Schwingenschlögl, Band inversion mechanism in topological insulators: A guideline for materials design, Phys. Rev. B **85**, 235401 (2012).

[29] X. Wei, B. Zhao, J. Zhang, Y. Xue, Y. Li, and Z. Yang, Chern insulators without band inversion in $MoS_2$ monolayers with $3d$ adatoms, Phys. Rev. B **95**, 075419 (2017).

[30] K. F. Garrity and D. Vanderbilt, Chern insulator at a magnetic rocksalt interface, Phys. Rev. B **90**, 121103(R) (2014).

[31] P. Hohenberg and W. Kohn, Inhomogeneous electron gas, Phys. Rev. **136**, B864 (1964).

[32] W. Kohn and L. J. Sham, Self-consistent equations including exchange and correlation effects, Phys. Rev. **140**, A1133 (1965).

[33] P. E. Blöchl, Projector augmented-wave method, Phys. Rev. B **50**, 17953 (1994).

[34] J. P. Perdew, K. Burke, and M. Ernzerhof, Generalized gradient approximation made simple, Phys. Rev. Lett. **77**, 3865 (1996).

[35] V. I. Anisimov, J. Zaanen, and O. K. Andersen, Band theory and Mott insulators: Hubbard $U$ instead of Stoner I, Phys. Rev. B **44**, 943 (1991).

[36] S. L. Dudarev, G. A. Botton, S. Y. Savrasov, C. J. Humphreys, and A. P. Sutton, Electron-energy-loss spectra and the structural stability of nickel oxide: An LSDA+$U$ study, Phys. Rev. B **57**, 1505 (1998).

[37] T. Böker, R. Severin, A. Müller, C. Janowitz, R. Manzke, D. Voß, P. Krüger, A. Mazur, and J. Pollmann, Band structure of $MoS_2$, $MoSe_2$, and $\alpha$-$MoTe_2$: Angle-resolved photoelectron spectroscopy and *ab initio* calculations, Phys. Rev. B **64**, 235305 (2001).

[38] J. Neugebauer and M. Scheffler, Adsorbate substrate and adsorbate adsorbate interactions of Na and K adlayers on Al(111), Phys. Rev. B **46**, 16067 (1992).

[39] H.-J. Kim, C. Li, J. Feng, J.-H. Cho, and Z. Zhang, Competing magnetic orderings and tunable topological states in two-dimensional hexagonal organometallic lattices, Phys. Rev. B **93**, 041404(R) (2016).

[40] H.-J. Kim, VASPBERRY: Berry curvature calculation code for VASP output, https://zenodo.org/records/1402593.

[41] T. Fukui, Y. Hatsugai, and H. Suzuki, Chern numbers in discretized Brillouin zone: Efficient method of computing (spin) Hall conductances, J. Phys. Soc. Jpn. **74**, 1674 (2005).

[42] R. Kubo, Statistical-mechanical theory of irreversible processes. I. General theory and simple applications to magnetic and conduction problems, J. Phys. Soc. Jpn. **12**, 570 (1957).

[43] Y. Wang, B. Wang, R. Huang, B. Gao, F. Kong, and Q. Zhang, First-principles study of transition-metal atoms adsorption on $MoS_2$ monolayer, Physica E **63**, 276 (2014).

[44] P. Liu, Z.-Z. Qin, Y.-L. Yue, and X. Zuo, Structural, electronic, and magnetic properties of vanadium atom-adsorbed MoSe2 monolayer, Chin. Phys. B **26**, 027103 (2017).

[45] E. Uesugi, T. Uchiyama, H. Goto, H. Ota, T. Ueno, H. Fujiwara, K. Terashima, T. Yokoya, F. Matsui, J. Akimitsu *et al.*, Fermi level tuning of Ag-doped $Bi_2Se_3$ topological insulator, Sci. Rep. **9**, 5376 (2019).

[46] F. L. Deepak, H. Cohen, S. Cohen, Y. Feldman, R. Popovitz-Biro, D. Azulay, O. Millo, and R. Tenne, Fullerene-like (IF) $Nb_xMo_{1-x}S_2$ nanoparticles, J. Am. Chem. Soc. **129**, 12549 (2007).

[47] S. S. Ataei and A. Sadeghi, Robust broken-gap $MoTe_2/ZrS_2$ van der Waals heterostructure, Phys. Rev. B **106**, 245301 (2022).

[48] C. van Efferen, C. Murray, J. Fischer, C. Busse, H.-P. Komsa, T. Michely, and W. Jolie, Metal-insulator transition in monolayer $MoS_2$ via contactless chemical doping, 2D Mater. **9**, 025026 (2022).

[49] L. Liu, H. Huan, Y. Xue, H. Bao, and Z. Yang, Anisotropy-induced phase transitions in an intrinsic half-Chern insulator $Ni_2I_2$, Nanoscale **14**, 13378 (2022).

[50] P. Zhou, C. Q. Sun, and L. Z. Sun, Two-dimensional anti-ferromagnetic Chern insulator: $NiRuCl_6$, Nano Lett. **16**, 6325 (2016).

[51] H.-S. Lu and G.-Y. Guo, Strain and onsite-correlation tunable quantum anomalous Hall phases in ferromagnetic (111) $LaXO_3$ bilayers ($X =$ Pd, Pt), Phys. Rev. B **99**, 104405 (2019).

[52] Y.-J. Song, K.-H. Ahn, W. E. Pickett, and K.-W. Lee, Tuning ferromagnetic $BaFe_2(PO_4)_2$ through a high Chern number topological phase, Phys. Rev. B **94**, 125134 (2016).